PHYSICAL REVIEW A **90**, 041401(R) (2014)

Role of laser-driven electron-multirescattering in resonance-enhanced below-threshold harmonic generation in He atoms

Peng-Cheng Li,[1,2,*] Yae-Lin Sheu,[1] Cecil Laughlin,[3] and Shih-I Chu[1,4,†]

[1]*Center for Quantum Science and Engineering, and Center for Advanced Study in Theoretical Sciences, Department of Physics, National Taiwan University, Taipei 10617, Taiwan*

[2]*College of Physics and Electronic Engineering, Northwest Normal University, Lanzhou 730070, China*

[3]*School of Mathematical Science, University of Nottingham NG7 2RD, England*

[4]*Department of Chemistry, University of Kansas, Lawrence, Kansas 66045, USA*

(Received 18 March 2014; revised manuscript received 10 June 2014; published 22 October 2014)

We present an *ab initio* investigation of the below-threshold harmonic generation of helium (He) atoms in few-cycle infrared laser fields by accurately solving the time-dependent Schrödinger equation and Maxwell's equation simultaneously. We find that the enhancement of the below-threshold harmonic generation only occurs to near the resonance structure of He, for which this mechanism is in agreement with the recent experimental study [M. Chini *et al.*, Nat. Photonics **8**, 437 (2014)]. Moreover, we perform the quantum and semiclassical trajectories analysis, including both the atomic potential and the laser field, as well as the synchrosqueezed transform of the harmonic spectra. Our results reveal that several multirescattering trajectories contribute to the resonance-enhanced below-threshold harmonic generation.

DOI: 10.1103/PhysRevA.90.041401 PACS number(s): 32.80.Rm, 42.50.Hz, 42.65.Ky

High-order-harmonic generation (HHG) of atoms and molecules in intense laser fields, leading to the production of the coherent extreme-ultraviolet and attosecond pulses, has attracted much interest in the subject of ultrafast science and technology in the last decade [1–6]. The essential features in HHG, such as the above-threshold harmonic plateau and cutoffs, can be well understood by the semiclassical three-step model [7,8]. The HHG cutoff occurs approximately at the energy $I_p + 3.17U_p$, where I_p is the atomic ionization potential, and U_p is the ponderomotive potential. Furthermore, the strong field approximation (SFA) [9] has been commonly adopted for studying the HHG above the ionization threshold. However, due to its complete neglect of the intermediate bound states and the Coulomb interaction in the final state, the SFA is not accurate to describe the below-threshold harmonic generation (HHG below the ionization threshold). In this Rapid Communication, we present an *ab initio* study of the below-threshold harmonic generation by accurately solving the time-dependent Schrödinger equation (TDSE). To simulate the propagation effects, we also solve the Maxwell equation simultaneously.

Recently, as a promising method to produce vacuum-ultraviolet (VUV) frequency comb, the number of studies of HHG in the near- and below-ionization threshold has been increased considerably. Yost *et al.* [10] have studied the VUV frequency comb from below-threshold harmonic generation in xenon irradiated by an intense infrared laser field. They presented the first explicit VUV frequency comb structure beyond the third harmonic. In addition, Power *et al.* [11] have found that the generation of below-threshold harmonics is dominated by long trajectories, via a nonperturbative approach. Hostetter *et al.* [12] have extended the semiclassical three-step model with the atomic potential for the treatment of below-threshold harmonic processes in a model atom. Soifer *et al.* [13] have studied near-threshold HHG from the aligned molecules. More recently, Michael Chini *et al.* [14] have demonstrated a new regime of phase-matched below-threshold harmonic generation, for which the generation and phase matching [15] is enabled only near the resonance structures of the atomic target.

In this work, we study the dynamical role of the quantum trajectories in the resonance-enhanced below-threshold harmonic generation of He atoms in few-cycle infrared laser fields. The He atoms have been chosen particularly as the atomic medium for the below-threshold harmonic generation due to the following two main reasons: (i) The He atom possesses a deep ionization potential, which allows one to obtain the high-order below-threshold harmonic generation. For example, the single-electron transition energies for $1s^2$-$1s2p\ ^1P$ (21.22 eV) coincide with the harmonic 13 (H13) energy of the Ti:sapphire laser; and (ii) Popmintchev *et al.* [16] have pointed out that the He atoms are generally the best atomic medium experimentally for harmonic generation since the bright phase-matched supercontinuum spectra generation can evolve into the soft x-ray region. To analyze the quantum trajectories featured in the below-threshold harmonic generation, we first compute the quantum trajectories by a three-step classical model including the atomic potential. We then invoke a synchrosqueezed transform (SST) technique to obtain the time-frequency features of the HHG of He calculated by solving the TDSE and Maxwell's equation simultaneously. By comparing the classical trajectories analysis and the SST time-frequency profile of the HHG, we find that several multirescattering trajectories have a strong contribution in the generation of the resonance-enhanced below-threshold H13.

The single-atom HHG spectra can be calculated accurately and efficiently by solving the following TDSE by means of the time-dependent generalized pseudospectral method [17]. In order to achieve a high accuracy for the harmonic spectra of He, an angular-momentum-dependent model potential is

*lipc@nwnu.edu.cn
†sichu@ku.edu

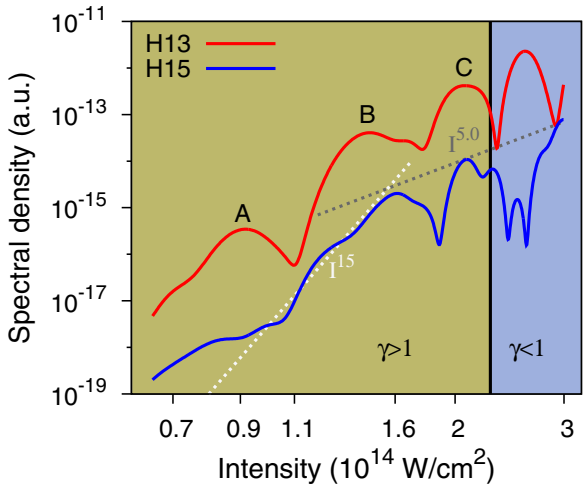

FIG. 1. (Color online) Spectra density of the below-threshold harmonic as a function of the laser intensity for the on-resonant H13 (red line) and the nonresonant H15 (blue line) of He driven by a few-cycle 760-nm laser pulse in the single-atom response. The γ is the Keldysh parameter. Note that the multiphoton ionization is typically classified by $\gamma > 1$, while tunneling ionization is classified by $\gamma < 1$. Both dashed lines indicate the harmonics yields as a function of the laser peak intensity I.

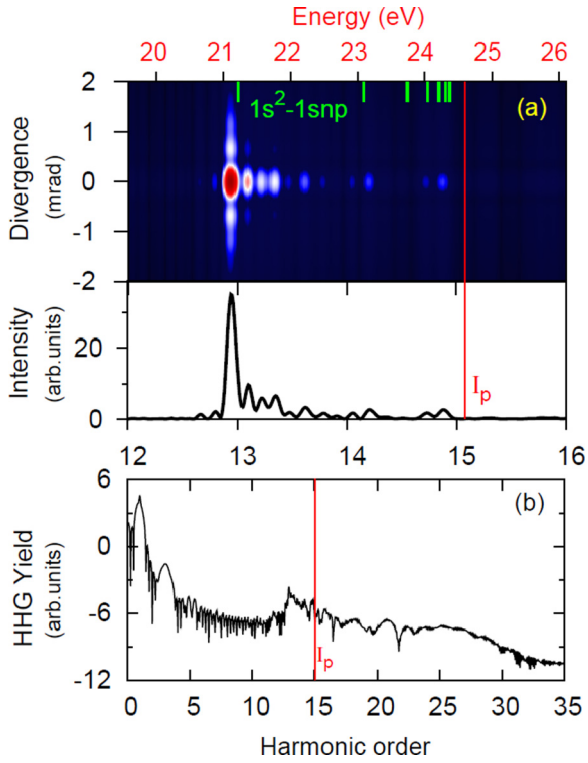

FIG. 2. (Color online) (a) Spatial distribution (upper panel) and the total intensity (lower panel) of He in the below-threshold regions. The laser peak intensity in the center of the gas jet is $I = 9.0 \times 10^{13}$ W/cm^2. The red solid line indicates the ionization potential I_p. The other parameters used are the same as those in Fig. 1. (b) Macroscopic HHG spectra in below-threshold and above-threshold regions.

constructed [18]. Once the time-dependent wave function $\psi(\mathbf{r},t)$ is available, the single-atom photon emission spectra can be calculated, within the semiclassical approach, by the following expression [19]:

$$S(\omega) = \frac{2}{3\pi c^2}|\widetilde{D}(\omega)|^2, \quad (1)$$

where c is the speed of light and $\widetilde{D}(\omega)$ is the Fourier transform of the time-dependent dipole acceleration.

Figure 1 shows the below-threshold harmonic spectra density as a function of the laser intensity for the on-resonant H13 and the nonresonant harmonic 15 (H15) of He atoms driven by a few-cycle 760-nm laser pulse in the single-atom level. The atomic ionization potential of He is equal to 0.904 a.u., so the harmonic 17 is just above threshold for the 760-nm laser pulse, which is similar to the laser pulse reported in recent experiments [14]. The main pulse sits on a pedestal of a weaker field (4% of the peak intensity) which also has a sine-squared shape and duration of 20 optical cycles. Thus the stronger field with four optical cycles is preceded by eight optical cycles and also followed by eight optical cycles of the weaker field. We know that the high-order-harmonic generation depends on both the single-atom response and macroscopic phase matching. However, in the low ionization and loose focusing case, the spectral features can be accurately described in the single-atom level. In Fig. 1, the H13 and H15 exhibit a different variation with laser intensity. Apparently there are several resonance-enhanced local maximum marked by A, B, and C for the below-threshold H13 when the Keldysh parameter γ ($\gamma = \sqrt{I_p/2U_p}$) is larger than 1, where the multiphoton ionization is dominant. Note that the local maximum harmonic yields of the H13 are located at the laser peak intensities $I = 9.0 \times 10^{13}$ W/cm^2, $I = 1.45 \times 10^{14}$ W/cm^2, and $I = 2.0 \times 10^{14}$ W/cm^2, respectively, and the corresponding yields are two orders of magnitude higher than those of near the below-threshold H15. In addition, the H15 harmonics yields as a function of the laser peak intensity I scaled as I^{15} in the intensity region of $\gamma > 1$ (multiphoton ionization regime), while this curve exhibits a change in slope in the intensity region of $\gamma < 1$ due to the tunneling ionization regime.

To demonstrate the macroscopic features of the resonance-enhanced below-threshold harmonic generation, we calculate the HHG spectra with the laser peak intensity $I = 9.0 \times 10^{13}$ W/cm^2 (marked by A in Fig. 1) by solving the TDSE and Maxwell wave equation [20–23] simultaneously. Figure 2(a) shows the spatial distribution of the below-threshold harmonic spectra (upper panel) of He. The confocal parameter of the laser beam is 10 mm, the length of the gas jet is 2.0 mm, the pressure is 10 Torr, and the target is set at the laser focus. We find that the yield of near the H13 is enhanced significantly since the 13 photons absorption energy of the 760 nm is equal to the transition energy of the $1s^2$-$1s2p$ ^1P (21.22 eV). Furthermore, the HHGs from the single-electron transitions $1s^2$-$1s3p$ ^1P (23.09 eV), $1s^2$-$1s4p$ ^1P (23.74 eV), and $1s^2$-$1s5p$ ^1P (24.05 eV) are also enhanced. Our results show that the generation of the enhanced below-threshold harmonic is enabled only near resonance structures of He, in agreement with the recent experimental mechanism [14]. The lower panel in Fig. 2(a) shows the corresponding total intensity

of the HHG calculated by integrating the spatial harmonics. It is clearly seen that the yield near the H13 is enhanced. Figure 2(b) shows the macroscopic HHG spectrum of He atoms including both the below-threshold and above-threshold regions, the cutoff is located at near the 29th order harmonic, and the low order harmonic emission is absent due to the simple atomic shell structure.

Next, we adopt a semiclassical three-step model [7,8] to analyze the contribution of the quantum trajectories in the resonance-enhanced below-threshold harmonic generation. In our calculations, the classical results are obtained by solving the Newton's equation, which is given by

$$\ddot{\mathbf{r}} = -\nabla V_l - E(t)\mathbf{e}_z, \tag{2}$$

where V_l is the angular-momentum-dependent atomic potential and $E(t)$ is the laser field. Figure 3 (a) shows the classical returning energy as a function of the ionization time (black line) and the return time (green line). Note that the returning energy includes the kinetic energy and the potential energy, and thus may become negative below the ionization threshold. For clarity, we only show the classical simulations in which the electrons are released in the first half cycle before the pulse peak. It is clearly seen that the HHG originated from two quantum trajectories, namely, the short trajectories (the higher harmonics are emitted after the lower ones) and the long trajectories (the higher harmonics are emitted before the lower ones). We find that the long-trajectories electrons associated with the multirescatterings (see the black dashed arrow) contribute to the near- and below-threshold harmonics 13–15, and the corresponding travel time is larger than one optical cycle.

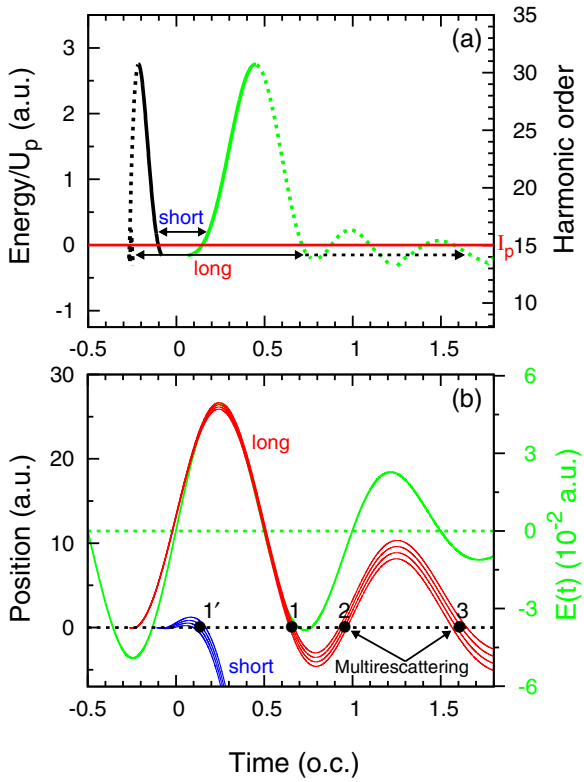

FIG. 3. (Color online) (a) Classical returning energy as a function of the ionization time (black line) and return time (green line), assuming initially the electrons with a small initial velocity are released at the core. (b) Position vs time in near- and below-threshold regions. Several typical rescatterings are marked by 1′ (short) and 1 (long), and multirescattering trajectories are marked by 2 (second return) and 3 (third return). The green solid line indicates the corresponding laser fields, and the laser parameters used are the same as those in Fig. 2.

Figure 3(b) shows the position of the electrons as a function of the time in the near- and below-threshold regions; the corresponding initial condition is marked by the arrows in Fig. 3(a). Namely, initially the electrons with a small velocity are released along (or against) the laser field direction at the core; here the minimum of initial velocity is $v_0 = 0$ and the maximum is the height of the barrier at the time of release, and typically the initial velocities used are $|v_0| \leqslant 1.0$ (in a.u.). We find that the maximum energy of the HHG is located at around the 29th harmonic, in good agreement with the harmonic spectra shown in Fig. 2(b). The short-trajectories electrons (marked by 1′) are allowed to quickly revisit the core with a short travel time (around 0.3 optical cycles), which coincides with the local peak of the laser field (see the green solid line). The long-trajectories electrons have multiscattering behaviors, and the first return (marked by 1) have the travel time around 1.0 optical cycle. However, the multirescattering process marked by 2 (second return) and 3 (third return) have a long travel time (>1.2 optical cycles). Indeed, to end the first return marked by 1, the electrons still move along the electronic field, which allows them to quickly return to the core at near the peak intensity in around 0.2–0.3 optical cycles (marked by 2); then the electrons continue to move along another side of the potential barrier and are allowed to return to the core in around 0.6 optical cycles (marked by 3).

To confirm that the multirescattering strongly contributes to the generation of the below-threshold on-resonance harmonic, as predicted by the semiclassical approach, we calculate the probability of the electrons with the corresponding return time t and return energy E as shown in Fig. 4 by using an extended semiclassical method [24], which can be obtained from the

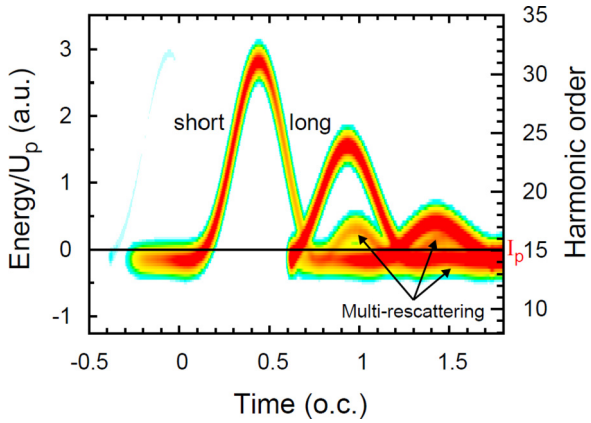

FIG. 4. (Color online) Semicalssical returning energy map. Note that the probability of the electrons with the corresponding return time and return energy is calculated by using an extended semiclassical method introduced in Ref. [24]. The black solid line indicates the ionization potential I_p.

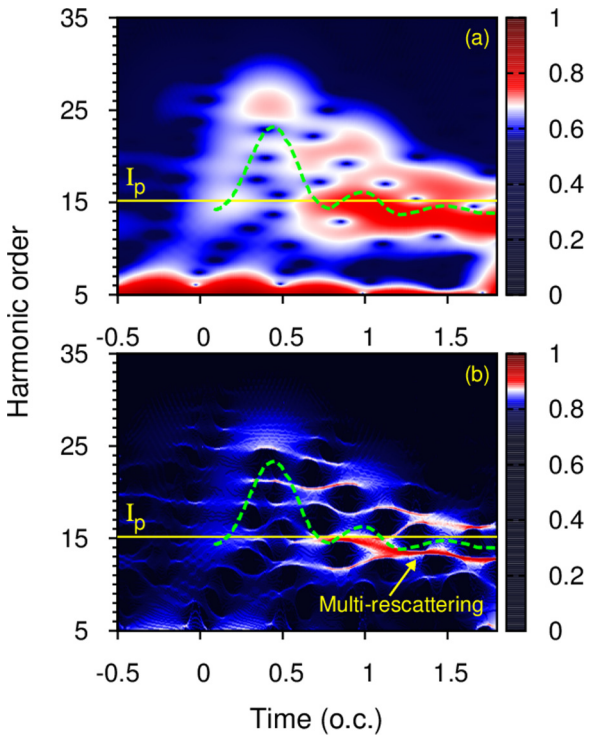

FIG. 5. (Color online) (a) Gabor time-frequency analysis of the harmonic spectra of He. (b) SST time-frequency analysis of the harmonic spectra of He. The laser parameters used are the same as those in Fig. 2. The green dashed line indicates the corresponding semiclassical result shown in Fig. 3(a) and the yellow solid line indicates the ionization potential I_p.

following expression:

$$\frac{dP(E,t)}{dEdt} = \int dt' d\mathbf{v} W(|E(t')|) P(\mathbf{v}) C_t(t', \mathbf{r}_0, \mathbf{v}, E_r, t_r) \times \delta(E - E_r)\delta(t - t_r), \quad (3)$$

where $W(|E(t')|)$ is the instantaneous tunneling ionization rate, E_r and t_r are the returning time and returning energy for given trajectories, and $P(\mathbf{v})$ is the Gaussian initial velocity distributions. Each trajectory is monitored for all the approaches to the parent ion. If an electron trajectory is such that it can return to the parent ionic core at time t_r with returning kinetic energy E_r, the factor $C_t(t', \mathbf{r}_0, \mathbf{v}, E_r, t_r)$ is set to 1. Otherwise, $C_t(t', \mathbf{r}_0, \mathbf{v}, E_r, t_r) = 0$. In Fig. 4, it is clearly seen that several multirescattering trajectories are superposed after the peak of laser field, leading to a contribution to the on-resonant H13.

Figure 5(a) shows the time-frequency analysis of the harmonic spectra of He by the Gabor transform [25], along with the corresponding semiclassical result in Fig. 2(a). However, from Fig. 5(a) it is difficult to recognize the contributions of the individual rescattering and multirescattering trajectories in the near- and below-threshold regions because several time-frequency profiles with different ionization peaks are superposed. To this end, we have also performed the time-frequency analysis methods based on the wavelet transform, Wigner-Ville transform [26], and SST [27,28]. We found that only the SST is capable of revealing the characteristic behaviors of harmonic spectra below the ionization threshold. The SST is defined by

$$S(t,\xi) = \int V(t,\omega) \frac{1}{\alpha} h\left(\frac{|\xi - \omega_f(t,\omega)|}{\alpha}\right) d\omega, \quad (4)$$

where $\alpha > 0$, $h(t) = e^{-t^2}/\sqrt{\pi}$, and $V(t,\omega)$ is the modified Gabor transform of the harmonic spectra, which can be written as

$$V(t,\omega) = \int d(t') g(t' - t) e^{-i\omega(t'-t)} dt', \quad (5)$$

where $d(t')$ is the time-dependent dipole moment. The instantaneous frequency information function $\omega_f(t,\omega)$ is defined by

$$\omega_f(t,\omega) = \begin{cases} \dfrac{-i\partial V(t,\omega)}{V(t,\omega)} & \text{for} \quad V(t,\omega) \neq 0 \\ \infty & \text{for} \quad V(t,\omega) = 0. \end{cases} \quad (6)$$

Figure 5(b) shows the SST time-frequency analysis of the harmonic spectra of He. By comparing with the classical calculation, it is clearly seen that the multirescattering trajectory marked by the yellow arrow has strong contributions to the near- and below-threshold harmonic 13–15; this result is in good agreement with the semiclassical result shown in Fig. 4. Particularly, several multirescattering trajectories are superposed at around 0.7–1.8 optical cycles, which contribute to the generation of the near- and below-threshold harmonics. Here the SST transform is introduced for the mechanism to the harmonic emission below the ionization threshold in the intense laser fields, and this method makes it possible to understand the working mechanism of the below-threshold generation.

In conclusion, we have presented an *ab initio* study on the below-threshold harmonic generation of He in few-cycle 760-nm infrared laser fields by solving accurately the TDSE and Maxwell wave equation simultaneously. An accurate angular-momentum-dependent model potential is constructed for the accurate description of the electron structure of the He atoms. Our results show that the macroscopic enhanced below-threshold harmonic generation is enabled only near resonance structures of He, in good agreement with the experimental mechanism. In particular, we find that the multirescattering trajectories have strong contributions to the resonance-enhanced below-threshold harmonic generation, and several multirescattering trajectories have a superposition after the peak of laser fields, leading to significantly enhanced on-resonant harmonics. This finding is confirmed by performing the extended semiclassical model simulations and the SST time-frequency analysis of harmonics spectra of He. Our results can provide a deeper understanding of the mechanism of resonance-enhanced below-threshold harmonic generation.

This work was partially supported by Chemical Sciences, Geosciences and Biosciences Division, Office of Basic Energy Sciences, Office of Science, US Department of Energy. P.-C.L. is partially supported by National Natural Science Foundation of China (Grants No. 11364039 and No. 11465016), Natural Science Foundation of Gansu Province (Grant No. 1308RJZA195), and Education Department of

Gansu Province (Grant No. 2014A-010). We also would like to acknowledge the partial support of Ministry of Science and Technology and National Taiwan University (Grants No. 103R8700-2 and No. 103R104021). The authors would also like to thank Dr. Hau-tieng Wu (Stanford University) and Dr. Tak-San Ho (Princeton University) for helpful discussions.

[1] E. Goulielmakis *et al.*, Science **320**, 1614 (2008).
[2] G. Sansone *et al.*, Science **314**, 443 (2006).
[3] J. Itatani, J. Levesque, D. Zeidler, Hiromichi Niikura, H. Pépin, J. C. Kieffer, P. B. Corkum, and D. M. Villeneuve, Nature (London) **432**, 867 (2004).
[4] R. Kienberger *et al.*, Science **297**, 1144 (2002).
[5] M. Drescher, M. Hentschel, R. Kienberger, M. Uiberacker, V. Yakovlev, A. Scrinzi, Th. Westerwalbesloh, U. Kleineberg, U. Heinzmann, and F. Krausz, Nature (London) **419**, 803 (2002).
[6] Michael Chini, Kun Zhao, and Zenghu Chang, Nat. Photonics **8**, 178 (2014).
[7] P. B. Corkum, Phys. Rev. Lett. **71**, 1994 (1993).
[8] K. C. Kulander, K. J. Schafer, and J. L. Krause, in *Super Intense Laser-Atom Physics*, edited by B. Piraux *et al.*, Nato Advanced Study Institute, Series B: Physics Vol. 316 (Plenum, New York, 1993).
[9] M. Lewenstein, P. Salières, and A. L'Huillier, Phys. Rev. A **52**, 4747 (1995).
[10] D. C. Yost, T. R. Schibli, J. Ye, J. L. Tate, J. Hostetter, M. B. Gaarde, and K. J. Schafer, Nat. Phys. **5**, 815 (2009).
[11] E. P. Power, A. M. March, F. Catoire, E. Sistrunk, K. Krushelnick, P. Agostini, and L. F. DiMauro, Nat. Photonics **4**, 352 (2010).
[12] J. A. Hostetter, J. L. Tate, K. J. Schafer, and M. B. Gaarde, Phys. Rev. A **82**, 023401 (2010).
[13] H. Soifer, P. Botheron, D. Shafir, A. Diner, O. Raz, B. D. Bruner, Y. Mairesse, B. Pons, and N. Dudovich, Phys. Rev. Lett. **105**, 143904 (2010).
[14] M. Chini, X. W. Wang, Y. Cheng, H. Wang, Y. Wu, E. Cunningham, P. C. Li, J. Heslar, D. A. Telnov, S. I. Chu, and Z. H. Chang, Nat. Photonics **8**, 437 (2014).
[15] A. Rundquist, C. G. Durfee III, Z. H. Chang, C. Herne, S. Backus, M. M. Murnane, and H. C. Kapteyn, Science **280**, 1412 (1998).
[16] T. Popmintchev *et al.*, Science **336**, 1287 (2012).
[17] X. M. Tong and S. I. Chu, Chem. Phys. **217**, 119 (1997).
[18] P. C. Li, C. Laughlin, and S. I. Chu, Phys. Rev. A **89**, 023431 (2014).
[19] L. D. Landau and E. M. Lifshitz, *The Classical Theory of Fields* (Pergamon, Oxford/New York, 1975).
[20] M. B. Gaarde, J. L. Tate, and K. J. Schafer, J. Phys. B **41**, 132001 (2008).
[21] V. Tosa, H. T. Kim, I. J. Kim, and C. H. Nam, Phys. Rev. A **71**, 063807 (2005).
[22] C. Jin, A. T. Le, C. A. Trallero-Herrero, and C. D. Lin, Phys. Rev. A **84**, 043411 (2011).
[23] P. C. Li and S. I. Chu, Phys. Rev. A **86**, 013411 (2012).
[24] J. J. Carrera, X. M. Tong, and S. I. Chu, Phys. Rev. A **74**, 023404 (2006).
[25] C. C. Chirila, I. Dreissigacker, E. V. van der Zwan, and M. Lein, Phys. Rev. A **81**, 033412 (2010).
[26] P. Flandrin, *Time-Frequency/Time-Scale Analysis* (Academic, New York, 1999).
[27] I. Daubechies, J. Lu, and H. T. Wu, Appl. Comput. Harmon. Anal. **30**, 243 (2011).
[28] Y. C. Chen, M. Y. Cheng, and H. T. Wu, J. R. Statist. Soc.: Ser. B **76**, 651 (2014).